Journal of Marine Research, 48, 729–763, 1990

The mesoscale variability of the sea surface temperature: An analytical and numerical model

by Patrice Klein[1] and Bach Lien Hua[1]

ABSTRACT

This study examines the emergence and evolution of a mesoscale sea surface temperature (SST) variability induced by a uniform and impulsive wind stress when an embedding quasigeostrophic (QG) flow is present. The SST variability which is triggered by the mixed-layer deepening closely resembles some characteristic properties of the QG flow, namely either the subsurface temperature or relative vorticity, depending on the amplitude of the deepening. The SST variance can have the same order of magnitude as the subsurface temperature variance. Within 10 days, the SST field, which is stirred only by the horizontal QG flow, displays a rapid spectral evolution characterized by the emergence of small-scale structures and the appearance of thermal fronts located in the QG jet areas. This evolution depends only on the deformation of the large-scale structures of the SST field, initially resulting from the mixed-layer deepening, by the QG strain field. In contrast with SST, later evolution of the mixed-layer depth is characterized by the emergence of large-scale structures. From these dynamical results, it is speculated that, when nonuniform initial conditions are considered, the resulting SST spatial variability should be more closely related to the subsurface temperature and the SST variance could be significantly increased.

1. Introduction

Mesoscale variability of the wind-driven mixed-layer (ML) is known to be induced by an embedding QG flow and/or by variable and intermittent atmospheric forcing (Large *et al.*, 1986; Weller, 1982). But so far, except in some particular regions such as the Gulf Stream region, the relative importance of these two factors is still unknown. In a first paper, Klein and Hua (1988), hereafter referred to as KH88, initiated a series of studies to investigate the specific effects of an embedding QG flow field on the spatial variability of the wind-driven ML. They focused on how the QG flow alone can induce a mesoscale variability of the ML dynamics and, in particular, of the ML depth and inertial motions. The present paper deals with the emergence and evolution of a mesoscale variability of the ML temperature (or SST since ML temperature is considered as vertically homogeneous) induced by the presence of a QG flow field.

1. IFREMER/CNRS, BP 70, 29280 Plouzane, France.

As in KH88, we have chosen to examine the simplest situation in order to isolate the interactions and physical processes involved. This is the situation of a ML embedded in a nonzero QG flow field. At the surface the ML is initially uniform with respect to temperature and depth, with no preexisting inertial motions. The atmospheric forcings—uniform and constant wind stress and surface heat fluxes assumed to be zero—cannot induce alone any variability of the ML. Then the ML response for 10 days is examined using the numerical model described in KH88. Note that, because of the short simulation duration (10 days) compared to the time scale associated with the QG flow (28 days), only a one-way influence of the embedding QG flow field on the ML dynamics can be considered.

Such an event, i.e., the 10 days response to a uniform wind stress, can be considered as characteristic of important transient events which control the time evolution of the wind-driven ML. When a QG flow is present, a ML mesoscale variability can emerge as the ML deepens, induced by a strong and impulsive uniform atmospheric forcing (Large *et al.*, 1986; KH88). Furthermore, because of the nature of strong atmospheric forcings, ML deepening is highly nonGaussian and intermittent in time (Elsberry and Camp, 1978, D'Asaro, 1985). Thereby, the ML mesoscale variability resulting from the ML deepening is likely to be affected, during the following days, only by advection processes, and mainly by the QG flow advection.

The relationship of the SST variability to the characteristics of the QG flow field, in particular to the vorticity and subsurface temperature, is assessed both analytically and numerically. Numerical experiments involve a QG flow field characterized by the presence of several energetic structures. This choice allows us to consider the results as statistically relevant and to examine their robustness in a more general situation. Some of the ideas used for this study have been taken from QG turbulence studies. However, whereas most of the related QG turbulence studies focus on a statistically equilibrated state, the state considered here is transient and of short duration. As will be seen, dynamical features of this transient state explain some discrepancies in the interpretation of satellite observations (Gower, *et al.*, 1980) with respect to theoretical results of two-dimensional turbulence (Lesieur and Sadourny, 1981), namely that measured spectra were too steep for a simple passive tracer.

The next section presents an analytical model of the emerging SST variability. Section 3 describes the numerical model used and the simulations performed. Section 4 examines the characteristics of SST variability resulting from ML deepening in two different situations. Section 5 focuses on the rapid spectral evolution of the SST field after ML deepening. Section 6 discusses the relevance and robustness of the results in more complex situations.

2. Analytical model of the influence of QG flow on SST

Using KH88's results and the framework of the QG theory, this section analytically investigates, in terms of the embedding QG flow properties, the characteristics of the

SST variability that appear in response to a strong uniform wind stress. As a preliminary, KH88's results concerning the effects of a QG flow on the ML dynamics are recalled and discussed.

a. ML dynamics equations

The situation considered is similar to that used in KH88. A ML of depth h, vertically homogeneous with respect to all properties is embedded in a QG flow (U,V). Because of the wind action, an additional horizontal velocity (u,v), associated with the inertial motions, is found within the ML and is supposed to be initially zero. In KH88, we studied only the response to an impulsive and uniform constant wind stress; radiative and turbulent surface heat fluxes are assumed to be zero. The ML dynamics equations related to this situation have been analytically derived, using the assumption that the Rossby number, ϵ (with $\epsilon \equiv U/fL$ where U and L are respectively a velocity and a length scale, and f is the Coriolis parameter), associated with the QG flow is much smaller than one. The resulting simplified equations which drive the ML dynamics in this situation, i.e., the equations for the Ekman transport, ML depth and ML temperature, have been carefully derived in KH88. Only the salient features of their derivation are recalled in this section.

i. Ekman transport. A first dimensional analysis of the different terms of the equations for the Ekman transport (hu,hv) showed that, with a uniform wind stress, the Ekman transport variability is of order $O(\epsilon)$. This led to the relation:

$$\{hu, hv\} \sim \frac{\tau}{f}[1 + O(\epsilon)]$$

with τ the modulus of the wind stress. Then, using this relation, a more detailed analysis of the nonlinear terms showed that the main effects of the QG flow on the Ekman transport evolution occur through the terms associated with the QG velocity gradients. These effects are of order $O(\epsilon)$ while other terms involved in the nonlinear advection terms were found to be of order $O(\epsilon^2)$. Consequently, when only terms of order $O(1)$ and $O(\epsilon)$ are retained, the resulting simplified equations driving hu and hv have been found to be:

$$\begin{aligned} \frac{\partial hu}{\partial t} + hu\frac{\partial U}{\partial x} + hv\frac{\partial U}{\partial y} - fhv &= \tau_x \\ \frac{\partial hv}{\partial t} + hu\frac{\partial V}{\partial x} + hv\frac{\partial V}{\partial y} + fhu &= \tau_y, \end{aligned} \tag{1}$$

where t is the time, x and y are the horizontal coordinates, respectively following east and north; τ_x and τ_y are the wind stress components normalized by the density ρ.

ii. ML depth. This equation is simply:

$$\frac{\partial h}{\partial t} + U\frac{\partial h}{\partial x} + V\frac{\partial h}{\partial y} + W + w_p + w_e = 0, \tag{2}$$

where $w_p = \partial hu/\partial x + \partial hv/\partial y$ is the inertial pumping and is calculated using (1); w_e is the entrainment (or the ML deepening) velocity and W the vertical velocity associated with the QG flow. Since, as in this study, the KH88 study focused on the mean evolution of the ML dynamics, only the mean values of w_p and w_e (i.e., averaged over an inertial period) have been considered. In KH88, the entrainment velocity has been parameterized by making the assumption that the main physical process involved in the wind-driven ML deepening is the current shear instability at the bottom of the ML (Pollard *et al.*, 1973; Price *et al.*, 1986). From this consideration a critical ML depth h_c, involving the maximum kinetic energy of the Ekman transport over an inertial period, has been defined and the entrainment velocity has been parameterized as:

$$w_e = \begin{cases} a(h - h_c) & \text{if } h < h_c \\ 0 & \text{if } h \geq h_c \end{cases} \tag{3}$$

where a^{-1} is an e-folding time which characterizes the deepening process ($a \sim f$). Then, using the analytical solution of (1) to calculate the maximum kinetic energy of the Ekman transport over an inertial period, and after a scaling analysis using the Rossby number ϵ, the expression for the critical ML depth, h_c, was found to be:

$$h_c = h_{c0}\left[1 + \frac{2}{3}\frac{\epsilon}{|\tau|^2}\left(\tau_x^2\frac{\partial U_*}{\partial y_*} - \tau_y^2\frac{\partial V_*}{\partial x_*} - 2\tau_x\tau_y\frac{\partial U_*}{\partial x_*}\right) + O(\epsilon^2)\right] \tag{4}$$

where

$$h_{c0} = \left[\frac{Ri_c}{g\dfrac{\Delta\rho}{\rho}}\frac{4|\tau|^2}{f^2}\right]^{1/3}.$$

Variables denoted by asterisks are nondimensional variables; Ri_c is a critical Richardson number and g, the gravity constant. The density jump Δ_ρ, which characterizes the stratification just below the ML, has been considered as uniform and constant during the entrainment process. This simplification, made after the observations and discussion from Price *et al.* (1986), allows an analytical parameterization of the entrainment.

The Ekman transport divergence, averaged over an inertial period, has been derived using (1). Its expression has been found to be:

$$w_p = \frac{\epsilon}{fL}\left[-\tau_y\frac{\partial \xi_*}{\partial x_*} + \tau_x\frac{\partial \xi_*}{\partial y_*}\right] \tag{5}$$

where ξ is the vorticity of the QG flow ($\xi \equiv \partial V/\partial x - \partial U/\partial y$).

iii. SST evolution. This equation is:

$$\frac{\partial \theta}{\partial t} + (u + U)\frac{\partial \theta}{\partial x} + (v + V)\frac{\partial \theta}{\partial y} - \frac{w_e}{h}(\theta - \theta_o) = 0 \tag{6}$$

where θ is the SST, and θ_o the temperature below the ML base.

b. Discussion of KH88's results

From the KH88 analysis, the effects of a QG flow on the Ekman transport (cf. Eq. 1) occur through the strain and deformation components of the QG velocity field and are of order $O(\epsilon)$. It was shown that one physical effect of these terms is to shift the local frequency of the inertial response to a higher or lower value, the difference being equal to half the QG vorticity. The other effect is to modify the maximum amplitude of the Ekman transport through the shear of the velocity component, which is parallel to the wind stress. This leads to an anisotropy of the QG flow influence along the wind stress direction. It should be noted that strong evidence of these effects has been provided by Niiler (1969) and, later, by the theoretical and observational studies from Weller (1982) and Kunze (1985).

The first consequence of the QG flow effects is the modification of the entrainment velocity w_e, by a spatially variable critical ML depth (cf. Eq. 4). Another consequence, analyzed in KH88, is the resulting ML deepening anisotropy that leads to large horizontal gradients of the ML depth in regions of QG jets parallel to the wind stress direction. Numerical results showed that the ML depth variability resulting from the ML deepening period has a significant RMS value, ~10% of the average ML depth. However the ML depth field was nonGaussian, intermittent, and characterized by a well marked anisotropy along the wind stress direction. Its correlation with the strain field and, in particular, with the vorticity was found to be significant, which led us to label the ML depth field a wind-biased vorticity mirror.

An analysis of the order of magnitude of the different terms involved in (2) showed two characteristic periods of the ML response. The first period is the first two days, when the entrainment process w_e is dominant; this period has been called the *ML deepening period.* The second period refers to the following days when the entrainment is no longer dominant and eventually disappears if the wind stress is stopped. The advective processes (through the divergence of the QG flow and Ekman transport) are then dominant and this period has been called the *advective period.*

In KH88, the wind stress was kept on during the advective period. Consequently, both entrainment velocity and advective terms drove ML depth evolution, and no detailed investigation of the separate effects of inertial pumping and of QG flow divergence was undertaken. In this paper, we have chosen to consider a strong wind event acting only during a short time (1 or 2 days). The initial motivation for this choice was to match a realistic situation such as the passage of an intense atmospheric front. However, in this particular situation some interesting effects of the QG flow divergence of ML depth evolution were revealed, which were not suspected in KH88.

These effects are examined in the next sections, and their consequences on the SST variability in a more general situation are discussed in Section 6.

c. Fundamental results for the SST

Both a dimensional analysis of the SST equation and the numerical results of KH88 have shown that SST evolution is characterized by two periods: the ML deepening period dominated by the effects of the one-dimensional vertical heat flux $w_e(\theta - \theta_o)$, and the advective period when the horizontal advective terms are dominant. For the sake of simplicity, the subsurface quantity θ_o in the KH88 study was assumed to be spatially uniform since it referred to a general passive tracer. However, when the θ_o-field refers to the subsurface temperature, it is not uniform when an evolving QG flow is present. The subsurface temperature is a linear combination of the baroclinic modes of the QG flow, leading to warm temperature in anticyclonic eddies and cold temperature in cyclonic ones. Thus the mesoscale variability of the subsurface temperature should affect the mesoscale variability of the heat injection, through the vertical heat flux $w_e(\theta - \theta_o)$. This study examines the evolution of the SST variability when a nonuniform subsurface temperature field is present. This is the main novel ingredient which is introduced into the situation of the KH88 study. As mentioned before, the atmospheric forcings differ from KH88 in that the impulsive uniform wind stress is stopped after 2 days. As in KH88 the initial conditions concerning the ML (i.e., h_i and θ_i) are assumed to be uniform over the whole domain.

During the ML deepening period, because of the dominance of one-dimensional vertical processes, the heat budget can be considered as local and be written as: $h\theta = h_i\theta_i + (h - h_i)\theta_o$. The characteristics of the emerging SST variability are linked to characteristics of both the subsurface temperature and the ML depth variability. Using the relations: $\theta' = \theta - \bar{\theta}$, $\theta'_o = \theta_o - \bar{\theta}_o$, $h' = h - h_{co}$ (where the overbar denotes the average over all the horizontal domain), if the fluctuations are small compared to the mean values the local heat budget leads to:

$$\theta' = \frac{(h_{co} - h_i)}{h_{co}}\theta'_o - \frac{h_i\Delta\theta_i}{h_{co}}\frac{h'}{h_{co}}. \tag{7}$$

As a consequence, the variance is:

$$\sigma_\theta^2 = \underbrace{\left(\frac{h_{co} - h_i}{h_{co}}\right)^2 \sigma_{\theta_o}^2}_{1} + \underbrace{\left(\frac{h_i\Delta\theta_i}{h_{co}}\right)^2 \cdot \frac{\sigma_h^2}{h_{co}^2}}_{2} - \underbrace{2\frac{h_{co} - h_i}{h_{co}} \cdot \frac{h_i\Delta\theta_i}{h_{co}}\frac{\overline{\theta'_o h'}}{h_{co}}}_{3}, \tag{8}$$

where $\Delta\theta_i = \theta_i - \bar{\theta}_o$.

Expressions (7) and (8) show that the relative contributions of the subsurface temperature and ML depth to the SST variability are strongly dependent on the ML initial conditions (h_i and $\Delta\theta_i$) with respect to the atmospheric forcings (through h_{co}). If we focus on the ML deepening, it is clear from (7) that when $h_{co} - h_i$ is large,

subsurface temperature variability strongly determines the SST variability, and when $h_{co} - h_i$ is small, ML depth variability is the determinant factor.

A more precise characterization of the SST variability during the ML deepening period can be undertaken in terms of the QG flow properties. An examination of the variability of the ML depth h leads to the approximation: $h'/h_{co} \sim -\epsilon\xi_*$, where ξ_* is vorticity (see KH88). Again, variables denoted by asterisks are nondimensional quantities. On the other hand, the subsurface temperature variability is related to the QG streamfunction field φ ($\varphi \equiv P/f_o\rho$ with P the pressure) by: $\theta'_o \sim (\epsilon F/\alpha)\,(\partial\varphi_*/\partial z_*)$, with $F \equiv f^2L^2/gD$ (cf. Pedlosky, 1987) and α the thermal expansion coefficient. Using these two relations, (7) can be written as:

$$\theta' \sim \epsilon\Delta\theta_i\left[\alpha_1 F_s\frac{\partial\varphi_*}{\partial z_*} + \alpha_2\xi_*\right] \tag{9}$$

with $\alpha_1 = (h_{co} - h_i)/h_{co}$ and $\alpha_2 = h_i/h_{co}$. F_s is a Froude number defined as: $F_s \equiv (f^2L^2)/(g\alpha\Delta\theta_i D)$.

The order of magnitude of the SST variability is directly proportional to the Rossby number ϵ. Moreover (9) shows that, when $\alpha_1 \sim \alpha_2$, the SST variability should resemble the potential vorticity of the QG flow vertically integrated over the surface layer, thus reinforcing the findings of Woods (1988) and Pollard and Regier (1990). However reality is more complex: SST variability is clearly linked to the vorticity and to the stretching of the QG flow in the surface layer, but the relative influence of the two strongly depends on the coefficients α_1 and α_2, i.e., on the amplitude of the ML deepening. When $h_{co} - h_i$ is small, the SST variability should resemble the QG vorticity, while if $h_{co} - h_i$ is large, the SST variability should resemble subsurface temperature. In an intermediate regime, the SST features will depend on the relative strength of $B \equiv (F_s\partial\varphi_*/\partial z_*)/\xi_*$; B, which is proportional to the equivalent of the local ratio of potential vorticity components (namely, the ratio of a vertically averaged stretching to the relative vorticity), is a local Burger number. Therefore, (9) shows the importance of both the local Burger number B and the ML initial conditions on the emerging SST variability. For example, in cyclonic eddies the vorticity ξ_* is positive while the subsurface temperature fluctuation $\partial\varphi_*/\partial z_*$ is negative; the resulting local SST value will be higher or lower than the mean value, depending on the ML initial conditions and on the value of B. Eq. (9) is the most important result for SST during the ML deepening period.

During the advective period, since the wind stress is stopped and the residual inertial motions are assumed to be negligible, the equations for the SST and ML depth evolution are the following:

$$\frac{D\theta}{Dt} = 0 \tag{10}$$

$$\frac{Dh}{Dt} + W = 0 \tag{11}$$

with $D/Dt = \partial/\partial t + U\,\partial/\partial x + V\,\partial/\partial y$, and U, V and W the QG velocity components. We can check from these two equations that the ML heat content over all the domain ($\overline{h\theta}$) is conserved when boundary conditions are periodic. However, these two equations differ by the presence of W, the vertical velocity associated with the QG flow, which leads to different asymptotic states for the SST field and for the ML depth field.

The SST equation (10) is simply the equation of a passive tracer stirred by a QG flow field. The asymptotic state of such a tracer is known to have a spectrum slope in k^{-1} and consequently its variance is dominated by small scales. From (10), the SST variance should be steady, insofar as diffusion processes are neglected. Consequently the asymptotic behavior will be characterized by a constant variance and a rapid development of the energetic small scales relatively to the large scales. On the other hand, (11) is simply the equation for the evolution of the depth of an isopycnal surface (cf. Pedlosky, 1987). More precisely, if an appropriate transformation is used, such as $h = (\alpha g/N^2)\chi$ with N the Brünt Väisälä frequency, then χ can be identified to θ_o, i.e., the subsurface temperature associated with the QG flow field (Pedlosky, 1987). Therefore the asymptotic state of the ML depth governed by (11) should be close to the spatial variability of the subsurface temperature (or the isopycnal topography). This means that during the advective period the ML depth variability should evolve from an image of the vorticity field toward an image close to the subsurface temperature field.

3. Numerical methodology

a. The coupled models

The numerical model used is identical to the one described in KH88. It concerns a simple ML model derived from the equations of Section 2a coupled to the QG model developed by Hua and Haidvogel (1986).

i. The Hua and Haidvogel (1986) QG model. This model is a **3 - D** spectral model which solves the potential vorticity equation:

$$\frac{\partial Q}{\partial t} + J(\varphi, Q) = -K\nabla^2\varphi|_{z=-H} - \nu\nabla^6\varphi + M \tag{12}$$

where the potential vorticity Q and the term M are:

$$Q(x, y, z, t) = \nabla^2\varphi + \frac{\partial}{\partial z}\left(\frac{f_o^2}{N^2}\frac{\partial\varphi}{\partial z}\right)$$

$$M = -\frac{\partial\varphi}{\partial x}\left(\beta - \frac{\partial}{\partial z}\left[\left(\frac{f_o^2}{N^2}\right)\frac{\partial U}{\partial z}\right]\right).$$

In addition, $f = f_o + \beta y$ is the Coriolis parameter, $N(z)$ the Brünt-Väisälä profile. K represents the friction coefficient through the bottom Ekman layer at $z = -H$, and ν is the hyperviscosity coefficient. The QG flow is forced by the baroclinic instability of a mean zonal flow U. A normal mode expansion has been used on the vertical, following Flierl (1978). The streamfunction, φ, is approximated by the truncated series:

$$\varphi(x, y, z, t) = \sum_{m=0}^{N_v} \psi_m(x, y, t) F_m(z)$$

where $F_m(z)$ is a solution of the Sturm-Liouville problem:

$$\frac{\partial}{\partial z}\left[\frac{f_o^2}{N^2}\frac{\partial F_m(z)}{\partial z}\right] = -\lambda_m^2 F_m(z),$$

and $\lambda_m^2 = (k_z)_m^2$ is the square vertical wavenumber associated with the m^{th} mode. The modal decomposition on the vertical allows production of a realistic QG flow in the upper layers for a given Brünt-Väisälä profile: the one chosen here is exponential and the total depth is $H = 5400$ m. The model uses 4 vertical modes ($N_v = 4$). The modal streamfunction components are periodic over the square domain $0 \leq x, y \leq 2\pi$. Accordingly, the streamfunction field is expanded in a Fourier series:

$$\psi_m(x, y, t) = \sum_{k=-N_h/2}^{N_h/2} \sum_{l=-N_h/2}^{N_h/2} \hat{\psi}_{mkl}(t) e^{i(kx+ly)}$$

where N_h is the number of horizontal modes. Oceanic measurements suggest that the most energetic scales are somewhat larger than the first Rossby radius of deformation R_d. If $k = 1$ is the scalar horizontal wavenumber associated with the size of the domain, the value $k = 7$ has been chosen for the wavenumber associated with the first radius of deformation. This means that the size of the domain is $14\pi R_d$. This size allows the presence of several energetic structures, and the field can be considered as statistically relevant. The horizontal resolution considered is 128×128 ($N_h = 128$). The numerical method used is described in Hua and Haidvogel (1986): the resulting equations have been integrated in time using a leapfrog differencing scheme for the advective terms, with periodic applications of a leapfrog trapezoidal step to diminish the computational mode. The nonlinear jacobian terms have been evaluated by using a spectral transform method introduced by Orszag (1971). Physical characteristics of the simulated QG flow are described in Section 3a.

ii. The ML model. The ML model has been built from Eqs. (2) through (6). The Ekman velocity u, v, averaged over an inertial period, is estimated from the analytical solution of (1) (Eqs. 7 of KH88). To be consistent with the QG model, horizontal diffusion processes, parameterized with a hyperviscosity coefficient, are added in Eqs. (2) and (6). The QG velocity components, U, V, and W, and the subsurface tempera-

ture, θ_o, are given by the QG model. Note that these quantities vary in space and time. The numerical method used follows the spectral numerical method of the QG model. In particular, variables are expanded in a Fourier series and the horizontal resolution is 128×128 ($N_h = 128$). At last, boundary conditions for the SST and ML depth are periodic.

b. Simulation parameters and initialization

i. Characteristics of the QG flow. As in KH88, the characteristics of the QG flow are close to those of the mesoscale flow of the Local Dynamics Experiment site (30° 05'N, 69° 30'W) where the mesoscale turbulence has been linked to the baroclinic instability of the mean Gulf Stream Recirculation flow (POLYMODE, 1986). In this region, the Coriolis parameter is $f_o = 0.75 * 10^{-4}\text{s}^{-1}$. The eddy kinetic energy per unit mass in the first 800 meters is 120 cm^2/s^2 and the first internal radius of deformation is $R_d \simeq$ 50 km.

The statistically equilibrated QG flow, corresponding to the above characteristics, chosen as the initial state for the simulations of this study, has been obtained using the Hua and Haidvogel (1986) model. Figures 1a and 1b show respectively the QG streamfunction in the upper layers and the kinetic energy spectrum corresponding to this initial state. An examination of the streamfunction field ten days later reveals a weak evolution of the QG flow. The kinetic energy spectrum of the QG flow has a peak wavenumber which corresponds to $k = 4$ and a spectrum slope of -4. The vorticity field (Fig. 1c) has a less steep spectrum slope (-2) and therefore contains more energetic small scales. The RMS value of the vorticity corresponds to an e-folding time of 1.5 day. Moreover, while the streamfunction is generally a Gaussian field (kurtosis value is 2.9), the vorticity is slightly intermittent (kurtosis value is 3.8). Figure 1d shows the subsurface temperature field, θ_o, in the upper layers ($z \sim -25$ m) at the initial time; θ_o is linked to the QG streamfunction $\varphi(x,y,z,t)$, given by the QG model, by the relation (Pedlosky, 1987):

$$\theta_o = \bar{\theta}_o + \frac{f_o}{g\alpha}\frac{\partial \varphi}{\partial z} \tag{13}$$

with $\bar{\theta}_o$ the mean temperature value just below the ML base. The chosen mean value, $\bar{\theta}_o$, is 16°C. The subsurface temperature mesoscale variability displays spatial features approximately similar to the streamfunction field. Subsurface temperature is colder in cyclonic eddies and warmer in anticyclonic eddies. The maximum temperature variation is 3°C and temperature variance is ~0.226(°C)^2, i.e., the same order of magnitude as that observed during LDE in the upper layers. The subsurface temperature spectrum displays a spectrum slope of $k^{-3.5}$ and therefore energetic large scales. Vertical velocity W is obtained by using the density equation, which leads in the QG

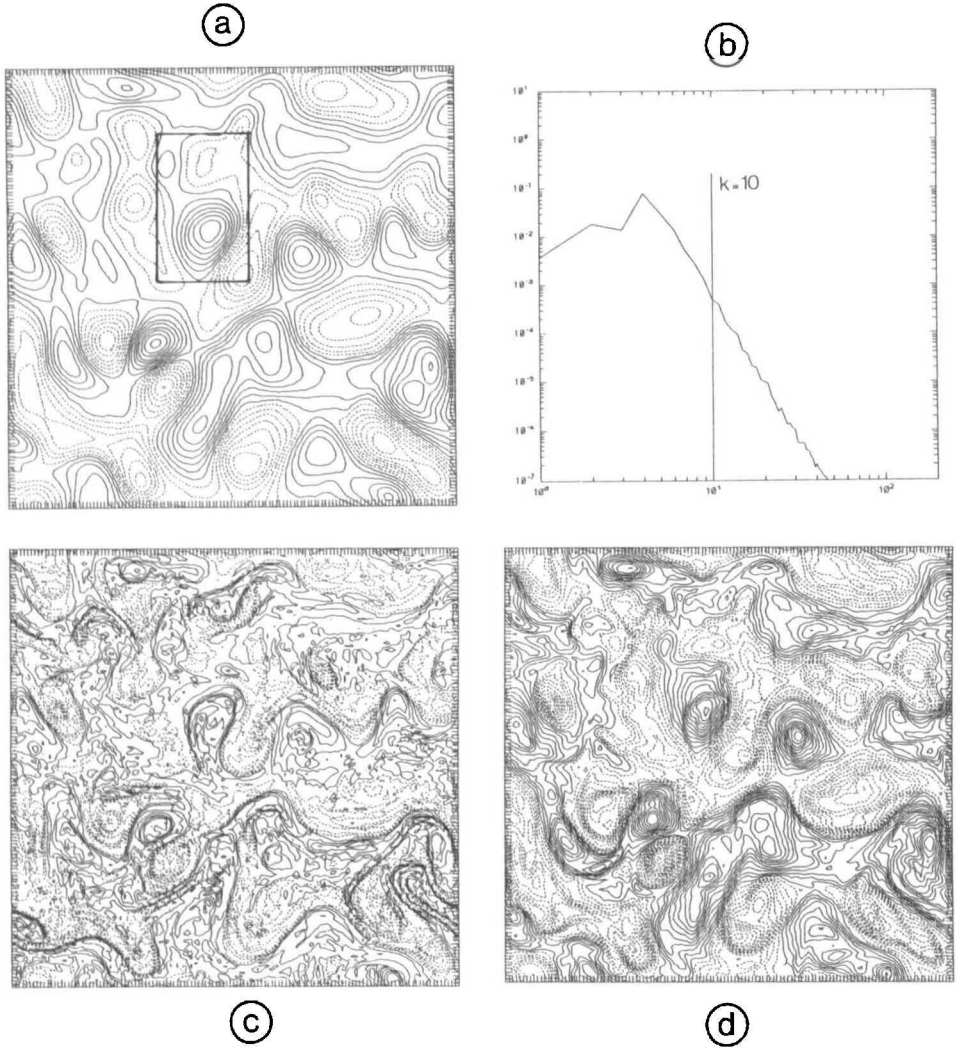

Figure 1. Contour maps (a, c, d) and spectrum (b) of the initial fields of the streamfunction (a, b), vorticity (c) and subsurface temperature (d). In (a, c, d), dashed and continuous contours correspond respectively to negative and positive values relative to the mean value. The sign convention is reversed for the vorticity contours for an easier comparison with other fields.

approximation to (Pedlosky, 1987):

$$W = -\frac{f_o}{N^2}\frac{D}{Dt}\left(\frac{\partial \varphi}{\partial z}\right) \tag{14}$$

where $D/Dt = \partial/\partial t + U\,\partial/\partial x + \mathrm{V}\,\partial/\partial y$ and with $N = [(-g/\rho)(\partial\rho/\partial z)]^{1/2}$ is the

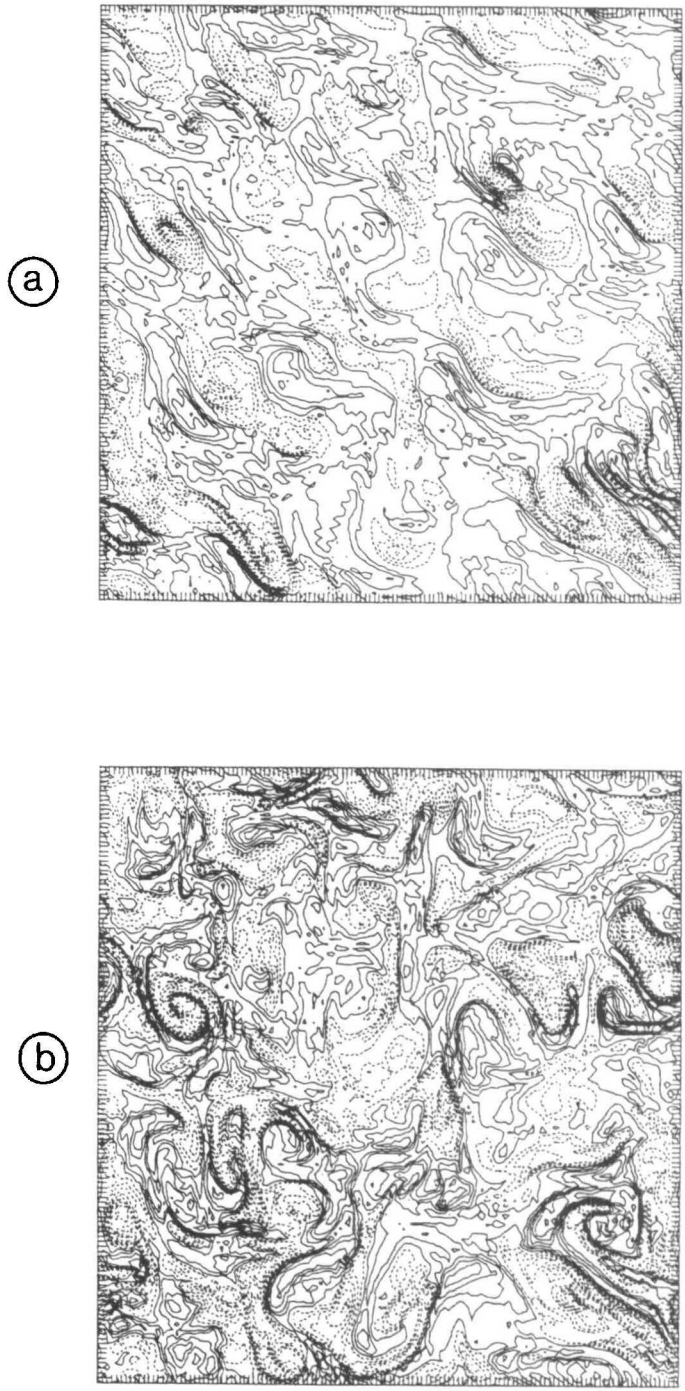

Figure 2. Contours maps (a, b) of the ML depth field respectively at $t = 2$ days (a) and $t = 10$ days (b) for simulation $\mathcal{L}$. Dashed and continuous contours correspond respectively to negative and positive values relative to the mean values. Contour intervals are 0.6 m in (a) and 0.7 m in (b).

Table 1. Statistics of the ML depth field for simulations $\mathcal{L}$ and $\mathcal{W}$. Subscripts 2 and 10 refer respectively to $t = 2$ days and $t = 10$ days. Units are in meters. The last column (σ_n^2) is the variance of ML depth horizontal gradient (in m/40 km) normalized by the ML depth variance.

Simulation	m	σ^2	Min.	Max.	Kurtosis	σ_n^2
$\mathcal{L}_2$	22.0	0.94	15.3	25.6	5.3	0.32
$\mathcal{L}_{10}$	22.0	2.30	13.9	26.6	3.8	0.28
$\mathcal{W}_2$	22.4	0.84	18.1	26.4	4.0	0.35
$\mathcal{W}_{10}$	22.4	2.17	16.3	27.2	3.4	0.29

Brünt-Väisälä frequency. Vertical velocity W has been calculated at the level $z = -25$ m using (14) and $\varphi(x,y,z,t)$ given by the QG model. The resulting W-field has an RMS value of ~0.36 m/day and a maximum variation of 2.5 m/day. These values are a little higher than those estimated from mooring data but are well within the range given by the QG approximation.

ii. ML characteristics. As mentioned before, ML initial conditions as well as the atmospheric forcings considered (i.e., the wind stress) are uniform over the whole domain in order to clearly identify the effects of the QG flow alone on the ML spatial variability. Moreover, the wind stress is held constant and uniform during the first two days and *is then turned off*. Residual inertial motions during the second period are assumed to be negligible in order to focus on the effects of the advection by the QG flow. The wind stress applied during the first two days corresponds to a northwest wind with a velocity of ~11 m/s, i.e.: $\tau_x = -\tau_y = 1.4 \times 10^{-4} \mathrm{m^2 s^{-2}}$. This amplitude is such that the mean critical ML depth h_{co} is equal to 22.3 m.

From the discussion of Section 2c on the influence of the ML initial conditions and atmospheric forcings (through h_{co}) on the SST variability, two sets of initial conditions, which differ only by the initial ML depth h_i, have been chosen. They correspond respectively to $h_i = 5$ m, leading to a large ML deepening ($h_{co} - h_i \sim 17$ m), and to $h_i = 20$ m, which leads to a weak ML deepening ($h_{co} - h_i \sim 2$ m). For both cases the initial ML temperature θ_i is uniform and equal to 20°C. Hence the mean temperature difference between the ML and the subsurface layers is $\Delta\theta_i = \theta_i - \bar{\theta}_o = 4$°C. Again there are no preexisting inertial motions within the ML in either case. The case of *large* ML deepening corresponds to a simulation called $\mathcal{L}$ and the one with a *weak* ML deepening corresponds to a simulation called $\mathcal{W}$. Figures 2a and 2b show the ML depth fields at the end of the ML deepening period and 8 days later for simulation $\mathcal{L}$. The ML depth field for simulation $\mathcal{W}$ has been found to be quite similar, which is not surprising since $h_{co} > h_i$ for both simulations. Statistical characteristics of this field are shown in Table 1. Comments on this field are similar to those given in KH88. Consequently, since this study is focused on the SST variability, only the effects of the ML depth variability on the SST variability and their contrasted evolution will be discussed. The results given in Sections 4 and 5 are for the SST variability at time $t = 2$

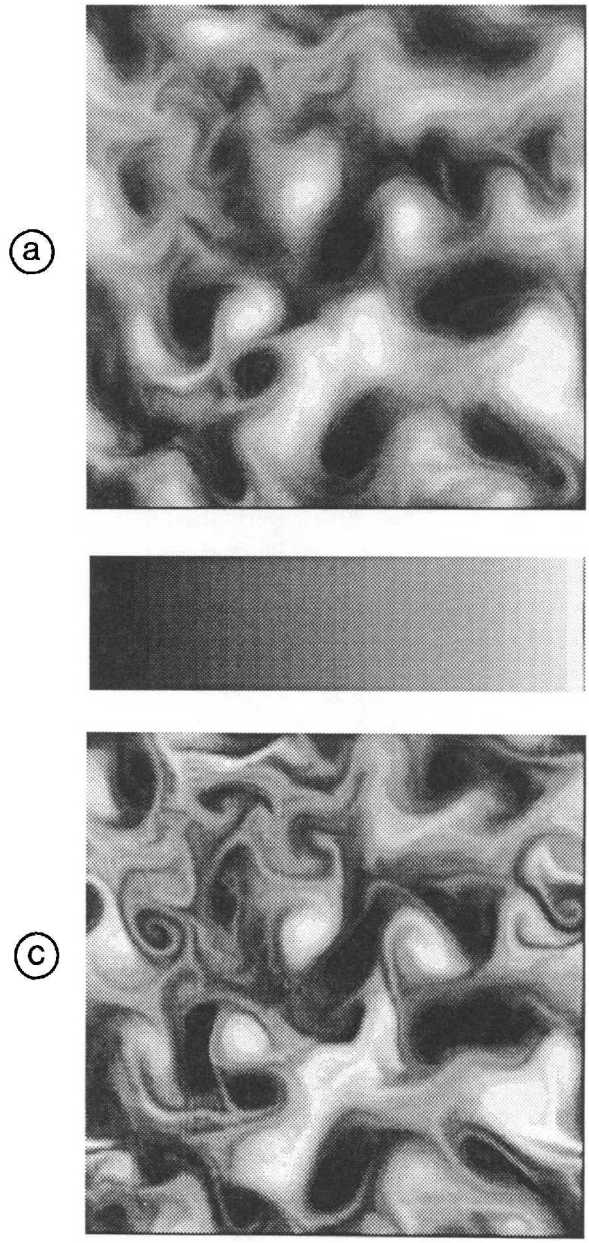

Figure 3. Digitized images (a, c), "energetic" areas (b, d) and high gradients areas (e) of the SST field for simulation $\mathcal{L}$ at $t = 2$ days (a, b) and $t = 10$ days (c, d, e). Grayscale ranges from the minimum temperature (black) to the maximum (white).

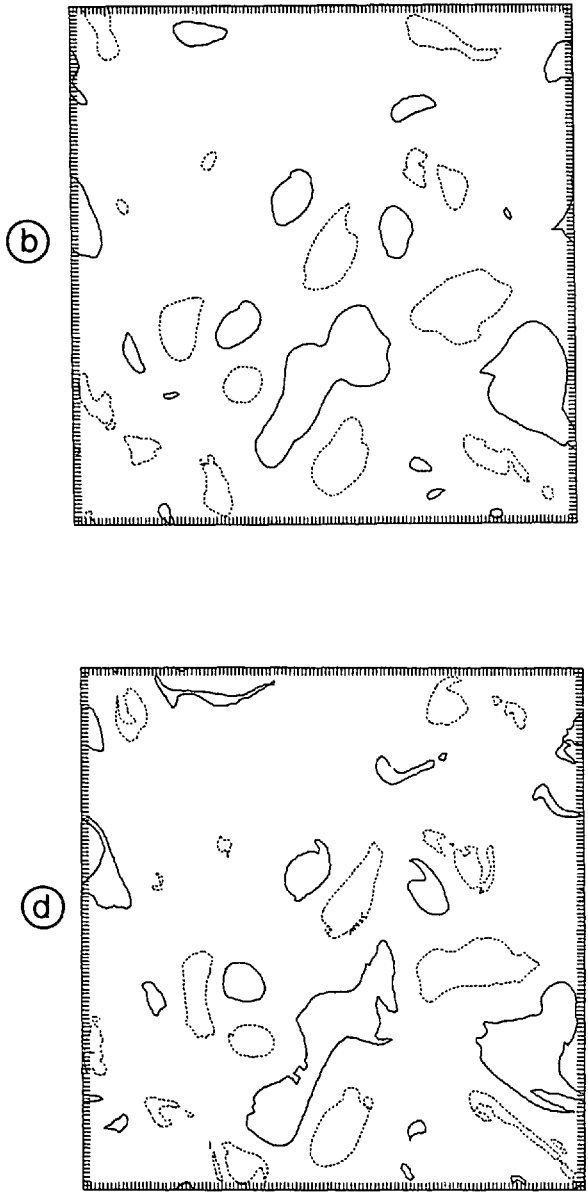

Figure 3. (Continued)

days, i.e., at the end of the ML deepening period, and at time $t = 10$ days that characterizes its evolution during the advective period.

c. Analysis through statistics and pattern identification

The SST spatial variability at the end of the ML deepening and 8 days later has been examined through its statistics and the statistics of its horizontal gradients as well as

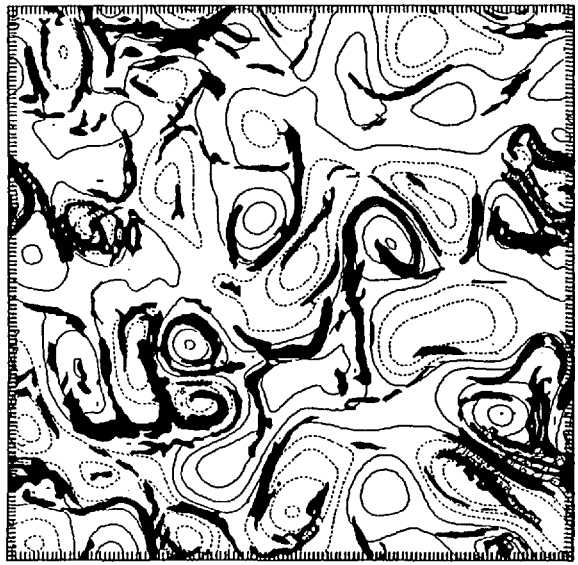

(e)

Figure 3. (Continued)

through its characteristics in the physical space. A spectral analysis to discriminate the spatial SST features into "large-" and "small-" scale structures has been performed. The term "large" scale has been used for the structures characterized by wavenumbers $k < 10$, whereas structures such that $k \geq 10$ have been called "small" scale structures. The choice of this critical wavenumber ($k = 10$), which corresponds to a length scale of ~200 km, allows us to distinguish the energy-containing scales, as displayed by the energy and enstrophy spectra, from the smaller scales (see Fig. 1b). The SST horizontal gradient modulus, $\frac{1}{2}[(\partial\theta^2/\partial x) + (\partial\theta^2/\partial y)]^{1/2}$, is expressed in °C/40 km.

Characteristics of the SST variability in the physical space have been examined by considering two classes of spatial patterns. In the first class are areas where the difference of SST value from the mean value is larger than a given threshold. The value for this threshold (which is 1.2 σ_θ, with σ_θ the SST RMS value) is chosen such that the areas concerned represent no more than 20% of the total area. These areas are called "energetic" since SST amplitudes in these areas are such that they capture a large part of the variance (more than 65% for a Gaussian field). The second class of patterns are areas where the modulus of the SST horizontal gradient is larger than a chosen critical value, corresponding to $r_c = m + 2\sigma$, with m and σ respectively the mean and RMS values of the SST horizontal gradient field at $t = 2$ days. This critical value is such that, at this time, these areas represent about 5% of the total area. The later evolution and growth of these areas during the advective period and their locations relative to the

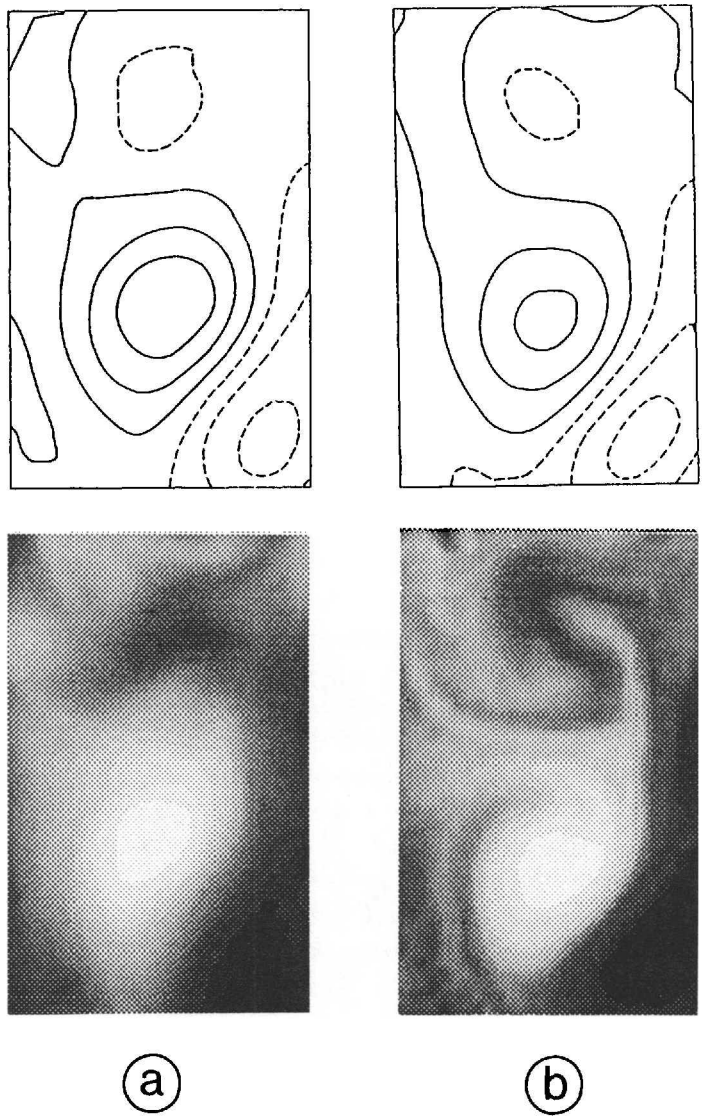

Figure 4. Zoom pictures of the QG streamfunction (upper part) and SST (lower part) fields for simulation $\mathcal{L}$ at $t = 2$ days (a) and $t = 10$ days (b). These pictures magnify the region identified on Figures 1a and 6.

QG streamfunction field reveal information about the efficiency of the stirring processes by the QG flow, as well as favorable locations for the subsequent formation of thermal fronts. These spatial patterns (energetic areas and high gradient areas) have been analyzed in terms of large- and small-scale structures. Such analysis is performed by comparing the fields with their truncated part (obtained after truncation of small

Table 2. Numerical results, at $t = 2$ days for simulations $\mathcal{L}$ and $\mathcal{W}$, of the SST variance and of the different terms (1), (2), (3) of Eq. (8).

Simulation	1	2	3	σ_θ^2	$\frac{(1+2+3)}{\sigma_\theta^2}$
$\mathcal{L}_2$	0.136	0.002	−0.016	0.138	~90%
$\mathcal{W}_2$	0.0026	0.0213	h−0.0085	0.0153	~99%

scales, i.e. scales corresponding to $k \geq 10$). Then a pattern is labelled a small scale structure if it does not exist anymore in the truncated field; otherwise the intersection of the pattern with its large scale component is examined to determine the relative contribution of the small scales with respect to the large scales.

4. SST variability at the end of the ML deepening period

a. The case of large ML deepening

Figure 3a shows a digitized image of the SST field for simulation $\mathcal{L}$ and the associated grayscale bar. This image reveals an almost equipartition of warm and cold large-scale patterns and the presence of a few filaments between them. Comparison with the streamfunction field, which at this time is very close to the one of Figure 1a, shows that the SST is warmer in anticyclonic eddies and colder in cyclonic ones. "Energetic" areas of the SST field, shown on Figure 3b, generally have an ovoid pattern and not surprisingly involve mainly large scales. A close comparison again shows a clear relation between these areas and the QG streamfunction field, with warm areas within anticyclonic eddies and cold ones in cyclonic eddies. Furthermore, these areas show a weak phase shift with the QG streamfunction field. The zoom pictures of Figure 4a illustrate the relationship, and in particular the weak phase shift, between the streamfunction and the SST.

Statistics show that the SST field is well correlated with the subsurface temperature field ($cor[\theta - \theta_o] = 0.952$) but is not correlated with h: the correlation with h is not negative (as should be expected from the sole effect of the ML deepening on the SST variability), but positive with a value of 0.44. This positive value indicates the significant correlation between θ_o and vorticity ξ. The negligible effect of the ML depth variability on SST for this particular simulation is explained by the values of α_1 and α_2 (respectively equal to 0.773 and 0.227). The relative contributions of the subsurface temperature and ML depth to the SST variance, as defined by (8), have been calculated from the numerical results and are shown in Table 2. First, the values show that relation (8) is correct within a 90% confidence level. This confirms a posteriori the dominance of one-dimensional processes in the SST evolution during the first two days. On the other hand, Table 2 also confirms that for a large deepening (simulation $\mathcal{L}$), ML depth variability has a negligible effect on the resulting SST variability. There-

Table 3. Statistics of the SST field for simulations $\mathcal{L}$, $\mathcal{W}$, $\mathcal{LF}$, $\mathcal{WT}$. Subscripts 2 and 10 refer respectively to $t = 2$ days and $t = 10$ days. Units are in (°C); m refers to the mean value and σ^2 to the variance. The last column refers to the fraction of the total variance contained in the small scales (corresponding to $k \geq 10$).

Simulation	m	σ^2	Min.	Max.	Kurtosis	Spectrum slope	$\sigma^2_{k\geq 10}/\sigma^2$
$\mathcal{L}_2$	16.63	0.138	15.54	17.91	2.99	−3.16	0.04
$\mathcal{L}_{10}$	16.63	0.136	15.52	18.02	3.01	−2.09	0.12
$\mathcal{W}_2$	19.58	0.015	19.07	20.06	4.1	−2.5	0.37
$\mathcal{W}_{10}$	19.58	0.013	19.09	20.15	4.3	−1.45	0.50
$\mathcal{LF}_{10}$	16.63	0.133	15.65	17.86	2.95	−2.44	0.07
$\mathcal{WT}_2$	19.58	0.009	19.27	19.94	3.53	—	0
$\mathcal{WT}_{10}$	19.58	0.009	19.26	19.98	3.66	−1.97	0.38

fore, SST variability is mainly dominated by the variability of the subsurface temperature. The variance of the SST field (Table 3) is almost half that of the subsurface temperature. Maximum variation is ~2.4°C. The field is Gaussian (kurtosis is ~3) and mainly dominated by large scales (spectrum slope is ~−3). The SST horizontal gradient field (Table 4) has a maximum value of ~0.5°C/40 km.

b. The case of small ML deepening

The SST field from simulation $\mathcal{W}$ (Fig. 5a) completely differs from the corresponding one of simulation $\mathcal{L}$. The digitized image reveals the presence of a large number of warm and cold filament-like structures but no large scale pattern emerges. Most of the energetic areas of this field (Fig. 5b) are characterized by much more elongated patterns than in simulation $\mathcal{L}$ (Fig. 3b), and are therefore much more affected by small scales. Furthermore, comparison of these energetic areas with the streamfunction field reveals a large disymmetry with the preceding simulation: many cold areas are within anticyclonic eddies, whereas many warm areas are in cyclonic ones. Last, these energetic areas display a larger phase shift with the QG streamfunction field than those of simulation $\mathcal{L}$.

Table 4. Same as Table 3 but for the SST horizontal gradients. Units are in (°C/40 km); σ_n^2 is the variance of SST horizontal gradient normalized by the SST variance.

Simulation	m	$\sigma^2(\times 100)$	σ_n^2	Max.	Kurtosis
$\mathcal{L}_2$	0.099	0.40	0.028	0.49	5.28
$\mathcal{L}_{10}$	0.155	1.50	0.110	1.27	10.85
$\mathcal{W}_2$	0.080	0.35	0.228	0.63	10.64
$\mathcal{W}_{10}$	0.101	0.62	0.470	0.67	7.33
$\mathcal{LF}_{10}$	0.118	0.81	0.061	0.72	7.1
$\mathcal{WT}_2$	0.032	0.04	0.042	0.14	5.0
$\mathcal{WT}_{10}$	0.067	0.28	0.306	0.47	7.6

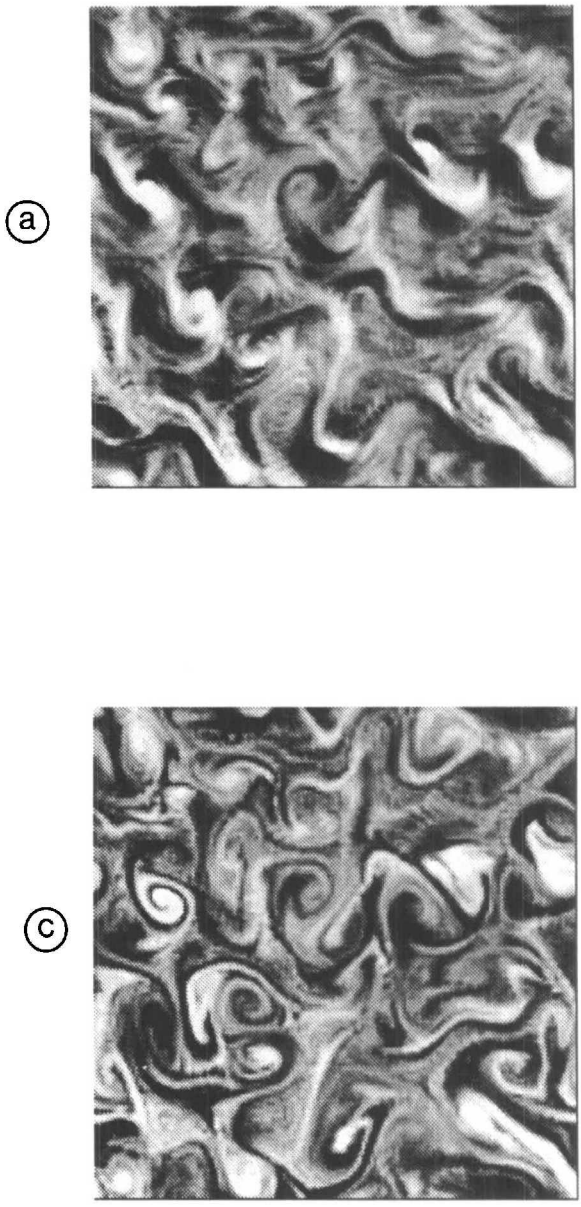

Figure 5. Same as Figure 3, except for simulation $\mathcal{W}$.

In fact, the SST field of simulation $\mathcal{W}$ is poorly correlated with the subsurface temperature field ($cor[\theta - \theta_o] = -0.166$) but is well correlated with the ML depth field: the corresponding correlation has now the right sign and is non-negligible ($cor[\theta - h] = -0.662$). As a consequence, the SST variability resembles the relative vorticity field ($cor[\theta - \xi] = -0.523$). This is again explained by the values of α_1 and

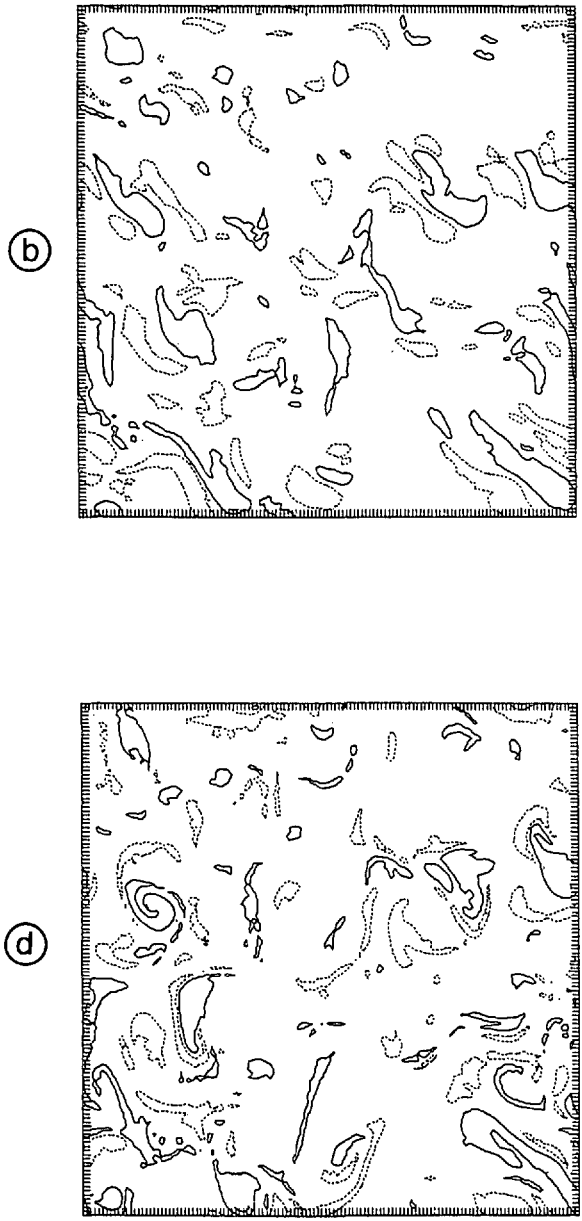

Figure 5. (Continued)

α_2 which are, in this simulation, respectively equal to 0.107 and 0.893. Table 2 shows that relation (8) is correct within a 99% confidence level, which again confirms the dominance of the one-dimensional processes. Furthermore Table 2 reveals that the contribution of the ML depth variability, in this simulation, is almost 10 times larger

than that of the subsurface temperature variability. These strong differences in the characteristics of the SST variability, observed in both simulations, result only from the different initial ML depth. The RMS value of the SST field is 3 times smaller than in the preceding simulation (Table 3). Its maximum variation is only 1°C and small scales represent a larger part of the variance, which is in accordance with the large number of filaments present on Figure 5a and with the less steep spectrum slope (~ -2.5). The SST gradient field has slightly smaller mean and RMS values than in the preceding simulation (Table 4), but the maximum value is larger (~0.63°C /40 km).

c. Discussion

As in KH88, the numerical results have confirmed the dominance of the one-dimensional processes during the first two days. The appearance of SST variability is only due to the spatial variability of the entrainment velocity (i.e., the variability of the critical ML depth) and of the subsurface temperature. Furthermore, these numerical results clearly show that the SST field statistically resembles the subsurface temperature field when the ML deepening is large, and the vorticity field when the ML deepening is small with eventually more intermittency and more energetic small scales. These two limits display some dissymmetry in the SST patterns relative to the eddy field and different spatial characteristics. Most of the "energetic" areas in simulation $\mathcal{L}$ are large scale structures, with a weak phase shift from the QG streamfunction field, and with warm areas in anticyclonic eddies and cold areas in cyclonic eddies. On the other hand, "energetic" areas in simulation $\mathcal{W}$ are much more affected by the small scales, with a larger phase shift with respect to the QG flow, and warm areas are in cyclonic eddies and cold ones in anticyclonic eddies.

The differences in the SST fields of simulations $\mathcal{L}$ and $\mathcal{W}$ are contrasted with the ML depth field (Fig. 2a) which, as mentioned before, is rather similar for both simulations. At the end of the ML deepening, this field is strongly correlated with the critical ML depth ($cor[h - h_{co}] = 0.95$) and close to the vorticity field ($cor[h - \xi] = 0.78$), with larger ML depth in anticyclonic eddies and smaller depth in cyclonic ones. Statistics (Table 1) show that its mean value is almost equal to the critical ML depth and the RMS value is non-negligible. However the field is intermittent (kurtosis is ~5) and the maximum amplitude variation reaches ~10 m. The maximum value of the ML depth gradient field attains 6 m/40 km.

It should be noted that an intermediate regime resulting from an intermediate magnitude of the ML deepening should be the most likely one. In such a regime (when $\alpha_1 \sim \alpha_2$ in Eq. 9), the relative influence of the ML depth and subsurface temperature fields on the SST field should depend, as discussed in Section 2c, on the *local values* of the Burger number $B = (F_s\, \partial\varphi_*/\partial_{z*})/\xi_*$. In other words, in such an intermediate regime, the SST variability will resemble the subsurface temperature variability in some areas and the vorticity variability in other areas, depending on the local Burger number B.

5. SST variability during the advective period

Between 2 and 10 days, i.e. during the advective period, both simulations $\mathcal{L}$ and $\mathcal{W}$ have revealed a fast evolution of the SST field. Such a fast evolution, which is due only to the QG flow advection processes, can be understood within the context of the studies of tracer dispersion in a 2-D turbulence field. Consequently a short review of these studies is undertaken in the next section.

a. General tracer dispersion in a QG turbulent field

Salient features of the studies related to the tracer dispersion problem in a 2-D turbulence field (cf. Moffatt (1981) and Rhines (1983) for a review) are that the tracer dispersion is characterized by a rapid cascade in wavevector space (from smaller wavenumbers to larger ones), which preferentially occurs in strain-dominated regions. These features imply that, in such a regime, energetic small scales of the tracer field have a short time duration and therefore come mainly from the interactions between the large scales of the tracer field (θ in our study) and the QG streamfunction field (φ) (see also Bennett, 1984). Hence the importance of the large scale part of θ and φ and of the phase shift between θ and φ, since the latter determines the efficiency of the interactions.

The role of the strain dominated regions on the tracer field evolution, and on the resulting cascade process, can be understood through the following analysis. When a tracer is conserved on a Lagrangian trajectory (as for the SST during the advective period), one way to examine its structural changes in terms of wavenumbers is to consider the time evolution of its horizontal gradients. From (10) this evolution is given by:

$$\frac{D}{Dt}\begin{bmatrix}\dfrac{\partial\theta}{\partial x}\\[2ex] \dfrac{\partial\theta}{\partial y}\end{bmatrix} = -\begin{bmatrix}\dfrac{\partial U}{\partial x} & \dfrac{\partial V}{\partial x}\\[2ex] \dfrac{\partial U}{\partial y} & \dfrac{\partial V}{\partial y}\end{bmatrix}\begin{bmatrix}\dfrac{\partial\theta}{\partial x}\\[2ex] \dfrac{\partial\theta}{\partial y}\end{bmatrix} \tag{15}$$

with $D/Dt = \partial/\partial t + U\,\partial/\partial x + V\,\partial/\partial y$ and U and V the QG velocity components. Using the approximation that the QG velocity gradients are slowly varying compared to the tracer gradient, solutions of (15), in the Lagrangian frame, have the form:

$$\begin{bmatrix}\dfrac{\partial\theta}{\partial x}\\[2ex] \dfrac{\partial\theta}{\partial y}\end{bmatrix} \sim \mathcal{M}\begin{bmatrix}\exp\left[-\dfrac{Q}{2}t\right]\\[2ex] \exp\left[+\dfrac{Q}{2}t\right]\end{bmatrix} \tag{16}$$

where $Q \equiv (S_1^2 + S_2^2 - \xi^2)^{1/2}$ with $S_1 \equiv \partial U/\partial x - \partial V/\partial y, S_2 \equiv \partial V/\partial x + \partial U/\partial y, \xi \equiv \partial V/\partial x - \partial U/\partial y$. $\mathcal{M}$ is a 2-D matrix involving the QG velocity gradients and the initial tracer horizontal gradient. Note that $\pm Q$ simply are the eigenvalues of the matrix in

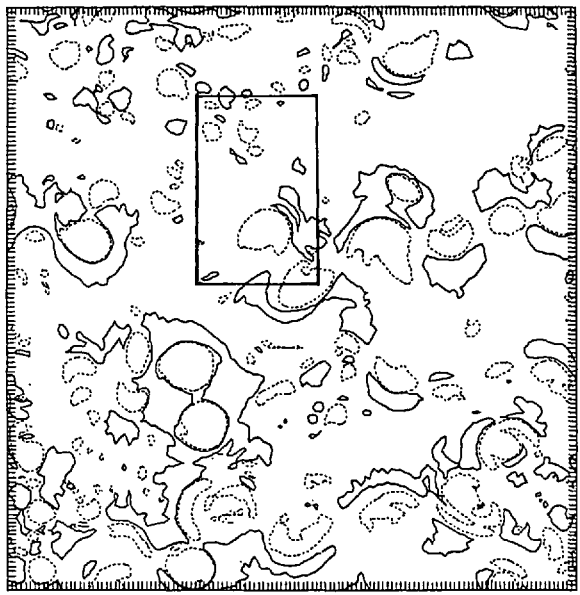

Figure 6. Spatial distribution of the areas corresponding to $|Q^2| > \sigma_{Q^2} / 2$. Dashed and continuous contours correspond respectively to negative and positive values.

(15) which involves the QG velocity gradients. Solution (16) is true for $Q \neq 0$; if $Q = 0$, as in the pure shear case, solutions are proportional to t (see Rhines, 1983).

Solution (16) shows that tendency of the *structural change* of the tracer field depends on the nature of the roots $\pm Q$ and then, in a 2-D turbulent field, on the spatial distribution of the strain and vorticity fields. Three classes of situations emerge, depending on the relative magnitude of strain and vorticity (Weiss, 1981; Rhines, 1983, McWilliams, 1984). First, in regions where $Q^2 < 0$, i.e., dominated by the vorticity (ξ), no significant or systematic growth of gradient, and thus no significant pattern change in terms of wavenumbers, can occur. These regions are labelled neutral and are generally located in eddy cores. Second, in regions where $Q^2 > 0$, i.e., dominated by the strain field (S_1, S_2), a systematic and significant growth of the tracer gradient can occur. These regions generally correspond to convergence or divergence zones of the streamfunction field. They are called turbulent because of the resulting pattern changes in terms of wavenumbers k, i.e., (from (16)) an exponential growth of one of the k-components and a damping of the other one—*hence the production of streaks and elongated filaments* in these regions. Third, in regions where $Q^2 = 0$ (as those corresponding to $S_1 = 0$, $S_2^2 = \xi^2$), only a weak growth of the gradients can occur (proportional to t). These regions, which generally correspond to a pure shear, are labelled jet areas. Thus structural changes in wavenumbers (or increase of gradients) of the tracer field mainly occur in strain dominated areas.

As an illustration, the Q^2-spatial distribution (Fig. 6) shows the most favorable areas

for the small scales production and the strongly neutral ones for the QG flow field considered in this study. As expected, a close comparison with the corresponding streamfunction field (which at this time much resembles the one displayed on Figure 1a because of its slow variation) reveals that negative regions are within an eddy core, whereas positive ones are located in convergence or divergence zones which are in the vicinity of strong vortices. Moreover, many of the positive regions tend to surround negative regions. Consequently the most active turbulence, leading in particular to an exponential growth of high SST horizontal gradients, should occur within these convergence or divergence zones in the close vicinity of the strong vortices, but it is excluded from the eddy cores. This clearly displays the importance of the phase shift between the tracer field and the streamfunction field: large scales of the tracer field will be all the more affected by the cascade process as their phase shift with the energy containing eddies (and therefore with the Q^2-field) is significant.

The time scale involved in the tracer cascade process can be inferred from the statistical properties of the quantity Q^2. In homogenous 2-D turbulence, Q^2 vanishes in the area integral (McWilliams, 1984) and when strain and vorticity fields follow a joint-normal distribution, the variances of Q_+^2 (i.e., Q^2-positive values) and Q^2 are directly related to the enstrophy (Hua, 1990):

$$\sigma^2_{Q^2_+} = \frac{1}{\sqrt{3}}\sigma^4_\xi, \qquad \sigma^2_{Q^2} = 3\sigma^4_\xi. \tag{17}$$

Hence tracer evolution is rapid because of the usually short time scale involved in the enstrophy. This link to the enstrophy time scale has previously been found by Kraichnan (1974) and Salmon (1980) who showed that the spectral evolution of a tracer field, for a transient regime, is characterized by an *exponential migration* of tracer variance from small k to large k with an e-folding time directly linked to the enstrophy. In our study, the time scale linked to the enstrophy corresponds to ~1.5 days, which is much smaller than the eddy time scale (~28 days). Furthermore the variances of Q_+^2 and Q^2 have been calculated and found to exactly satisfy (17). So the quantity $Q/2$ involved in (16) corresponds to an e-folding time of 2.4 days. This value is such that, in the most favorable areas, the SST-horizontal gradient can be multiplied by 3.5 within 3 days. Last, because of the order of magnitude of this e-folding time, the time duration of the advective period considered in this study (i.e., 8 days) should be large enough to display a significant SST evolution.

b. SST evolution as a transient tracer

i. The case of large ML deepening. Comparison of Figures 3a and 3c shows the evolution of the SST variability during the advective period for the simulation $\mathcal{L}$. The warmest and coldest areas of Figure 3c appear again to involve large scale features and are well related to the ones of Figure 3a. However, Figure 3c reveals the emergence, within 8 days, of a large number of filament-like structures. Most of these small-scale

structures appear to be attached to, and for some of them, to surround the more energetic SST large-scale features. More precisely, these filament structures seem to result from the deformation of the large-scale SST features. Such deformation is well displayed in some cases by the appearance of conspicuous "hammer heads" patterns. Figures 4a and 4b illustrate the rapid formation of such a pattern. The warm area of Figure 4a is closely related to the anticyclonic eddy with a weak phase shift. Eight days later, the SST spatial distribution inside the anticyclonic eddy is almost unchanged. This region corresponds to a $Q^2 < 0$-area with a strong Q^2-value in the south part of the eddy core (see Fig. 6). However, outside the anticyclonic eddy and in particular on its northern edge, the SST spatial distribution has experienced some significant evolution, leading to the appearance of cold and warm filaments. This evolution is explained by the positive Q^2-value in the area outside and around the eddy core and particularly on the northern edge (Fig. 6 shows only the strong positive Q^2-value in the eastern and northeastern part of the eddy core). Figure 3d displays the energetic areas extracted from the SST field. These areas are mainly dominated by the large scales and almost overlap the ones of Figure 3a (the overlap concerns more than 60% of the total surface of the energetic areas of Figure 3a). Only four of them (three in the upper part of Figure 3d and one in the lower right corner) have undergone some deformation and have an elongated pattern. Except for these four areas, most of the others have experienced a small deformation and change and, when compared with the streamfunction field (not shown), are again found to be inside QG vortices, with warm areas in anticyclonic eddies and cold areas in cyclonic eddies. Figure 3d shows almost no filament structures. This means that these small scale structures which have emerged within 8 days are not energetic in terms of the SST departure from the mean value.

The statistics (Tables 3 and 4) well corroborate these characteristics of the SST evolution during the advective period. The correlation between the SST field at the end of the ML deepening and the one 8 days later is high (~0.78): this confirms the weak evolution of the large scale energetic structures. Mean value and variance of the SST field have not changed within 8 days. However the spectrum slope has significantly changed and is less steep (it evolves from k^{-3} to k^{-2}), which reveals that the small scales rapidly become more energetic. The strong and rapid emergence of the small-scale structures is emphasized by the statistics of the SST horizontal gradients (Table 4). Mean value of the SST gradients is multiplied by ~1.6 and its variance by 4 within 8 days. Moreover the SST gradient field becomes more intermittent: its kurtosis value springs from 5 to more than 10. The maximum value attains ~1.3°C/40 km.

Examination of the SST gradient field in the physical space (Fig. 3e) illustrates the significant change due to the emergence of the small scales within 8 days. Areas where values are larger than 0.23°C/40 km (which is the value $m + 2\sigma$ at the end of the ML deepening period) springs from 4.5% to 20% of the total area within 8 days (Fig. 3e). These areas have a pattern close to a filament-like structure. Furthermore the comparison with the streamfunction field shows that the high SST gradient areas are

located on the edge of the strong QG vortices and in the vicinity of saddle areas. One can notice that, in the vicinity of many QG jets, there exist two high SST gradient areas, one on each side of the jet. Finally, these high SST gradient areas are mainly small-scale structures since they disappear when small scales (corresponding to $k \geq 10$) are truncated in the SST field.

Therefore, in this simulation, the energetic areas of the SST field, which initially involved large-scale structures and displayed a weak phase shift with the streamfunction field, experience slow changes and small deformations during the advective period. Yet these deformations, which occur on the edges of the QG vortices and in the vicinity of saddle areas, lead to the rapid emergence of much less energetic small-scale features and associated high gradient areas. Thus the SST evolution in this stimulation well illustrates the cascade process of a transient tracer as briefly described in section 5a.

ii. The case of small ML deepening. The SST field in simulation $\mathcal{W}$ appears to experience a more important evolution (see Figs. 5a and 5d). The warmest and coldest areas are affected by significant changes and deformations within 8 days: the corresponding areas of Figure 5c do not seem to match those of Figure 5a. Moreover Figure 5c reveals the appearance of a large number of filaments that seem much more energetic than in the preceding simulation. Many of these warm and cold filaments are paired and produce high SST contrasts. Analysis of the energetic areas extracted from the SST field (Fig. 5d) confirms the significant change of this field. These energetic areas (Fig. 5d) are weakly related to the initial ones (Fig. 5b) and appear to have experienced significant deformations. Many of them have become filament-like structures, which display the emergence of strongly energetic small scales.

The statistics confirm this significant SST field evolution within 8 days. The correlation between the SST field at the end of the ML deepening period and the one 8 days later is low (~0.23), which corroborates the large change and deformation of the energetic areas. The SST variance has slightly decreased within 8 days (Table 3). This indicates that the contribution of small scales to the variance (which reaches half of its value) is now significant enough for the SST variance to be affected by the diffusion processes. The large development of the small scales is shown by the evolution of the spectrum slope, which goes from $k^{-2.5}$ to $k^{-1.45}$. This development is emphasized as well by the large increase of the SST horizontal gradient variance, multiplied by ~1.8 within 8 days (Table 4). The SST horizontal gradient variance normalized by the SST variance (σ_n^2) has been calculated in order to quantify the importance of the small scales relative to the large scales. Variance σ_n^2 is simply the square of the radius of gyration of the SST spectrum. Its value for the SST field of Figure 5c is ~4 times larger than the corresponding value for the simulation $\mathcal{L}$ (Table 4). Moreover, at this time, the small-scale features (corresponding to $k \geq 10$) constitute 50% of the total SST variance instead of 12% only for the simulation $\mathcal{L}$.

Therefore, the SST field evolution in this simulation is characterized by a strong

deformation of the energetic patterns and rapid emergence and development of small-scale features that appear to be much more energetic than in the preceding simulation. This again illustrates the cascade process of a transient tracer. However, in this case, this process strongly affects the energetic scales and therefore seems to be more efficient than in the preceding case.

c. Mechanisms of the SST transient cascade

The different SST evolutions displayed by simulations $\mathcal{L}$ and $\mathcal{W}$ can be understood using the results of the tracer dispersion studies. From Section 5a, the rapid tracer cascade is driven by the time scale linked to the enstrophy and strongly depends on the large scales of the tracer field and their phase shift with the energy-containing eddies. The larger phase shift between the SST energetic areas and the streamfunction field which was found in simulation $\mathcal{W}$ at the end of the ML deepening can explain the larger efficiency of the SST cascade. However, while the initial SST energetic areas of simulation $\mathcal{L}$ were dominated by the large scales, the ones of simulation $\mathcal{W}$ were much contaminated by the small scales: the latter constitute 37% of the total variance instead of 4% in simulation $\mathcal{L}$ (see Table 3). Consequently, for a better characterization of the SST cascade mechanisms, we have investigated, through additional simple numerical experiments, the specific role of the large scales of the SST field on the transient SST cascade as well as the particular importance of the phase shift with the QG flow.

i. The predominent role of large scales. The specific role of the large scales of the SST field on the subsequent SST evolution has been examined through a simulation (named $\mathcal{WT}$) similar to $\mathcal{W}$, except that small scales (with $k \geq 10$) are truncated in the SST field at $t = 2$ days. The truncated SST field (Fig. 7a) strongly differs from the original one: the corresponding image (Fig. 5a) displays no filament-like structures and the extracted energetic areas (not shown) are large-scale structures characterized by a significant phase shift with the streamfunction field. Yet, 8 days later, the SST field of simulation $\mathcal{WT}$ (Fig. 7b) contains many energetic filament-like structures and resembles the SST field of simulation $\mathcal{W}$ (Fig. 5c). Note also the small scale "corrugated" patterns displayed by Figure 7b, which are more pronounced than on Figure 5c, but still have small amplitudes. Such "corrugated" patterns have also been observed in higher resolution models (McWilliams, 1989) and appear to have no important influence on other more energetic features. Analysis of the energetic areas at this time confirms the resemblance between the two SST fields: the corresponding areas of simulation $\mathcal{WT}$ (Fig. 7c), which are mainly small-scale structures, match well with the corresponding ones of simulation $\mathcal{W}$ (Fig. 5d): the overlap includes more than 65% of their surface. The SST statistics evolution in simulation $\mathcal{WT}$ shows the rapid development of the small scales within 8 days. The truncation, at the end of the ML deepening period, strongly reduces the SST variance (Table 3) by 1.5 and the SST horizontal gradient variance (Table 4) by 8.5. However, 8 days later, the small scales ($k > 10$)

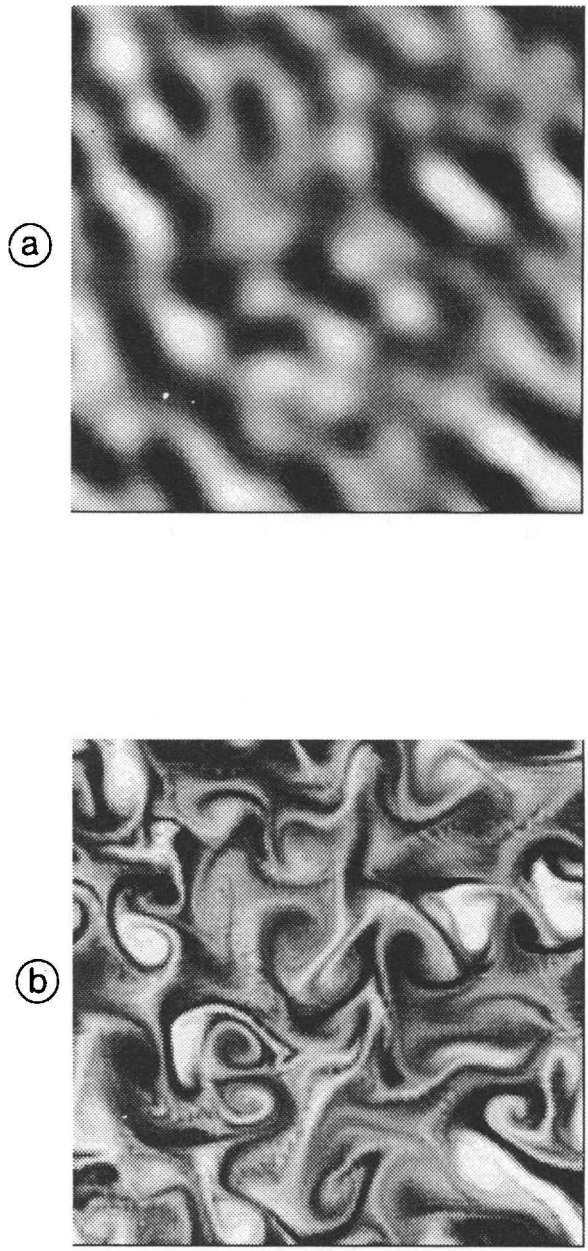

Figure 7. Digitized images (a, b) and "energetic" areas (c) of the SST field for simulation $\mathcal{WT}$ at $t = 2$ days (a) and $t = 10$ days (b, c). Grayscale ranges from the minimum temperature (black) to the maximum (white).

Figure 7. (Continued)

again contribute to a large part (38%) of the total SST variance and the variance of the SST horizontal gradients is multiplied by 7. Last, the normalized SST gradient variance (σ_n^2), initially reduced by a factor ~5 because of the truncation, compares well 8 days later with the reference simulation: the ratio is only ~1.5 (Table 4). Consequently these results show that most of the small scales, which emerge and are present 8 days after the end of the ML deepening period, come from the interaction of the *large scales* of the SST field with the QG flow field. The small scales of the SST field have almost no memory at a time scale of some days.

ii. Phase shift between the SST and the QG flow. One characteristic effect of the phase shift between the SST and the QG flow occurs through the influence of the time evolution of the QG flow, even if this evolution is quite slow. This specific influence has been examined using a simulation named $\mathcal{LF}$ which is similar to simulation $\mathcal{L}$ except that the velocity field is "frozen" during the advective period. Large differences with simulation $\mathcal{L}$ are found (cf. Tables 3 and 4): in particular the variance of the SST gradient field is reduced by a factor 2! Therefore, even on a quite short period, the slow time evolution of the turbulent QG flow field has a significant effect on the SST field evolution and thereby *the QG flow field cannot be assumed to be steady.* This significant effect is due to the phase shift between the QG flow and the SST field, which

is always changing because of the QG flow evolution, and which therefore is always different from zero, leading to a larger efficiency of the non-linear terms.

iii. Discussion. It is clear from Section 5a that the rapid SST evolution found in this study is explained by the short time scale linked to the enstrophy. However, the results of this section strongly emphasize that, on a time scale of a few days, the large-scale structures of the SST field and their locations relative to the energy containing eddies are mostly important for the efficiency of the SST cascade, insofar as the main SST energetic features are considered. This factor explains the different SST evolutions found in simulations $\mathcal{L}$ and $\mathcal{W}$ and also the significant effect of the slow time evolution of the QG flow field. These results show the importance of the initial SST variability and therefore the importance of the factors involved in the ML deepening, i.e., the ML initial conditions versus the atmospheric forcings and also the spatial distribution of the local Burger number B of the QG flow. Indeed, depending on whether the SST field resulting from the ML deepening is closer to the relative vorticity or to subsurface temperature, leading to large scale SST structures with a more or less large phase shift with the streamfunction field, the later development of the SST small scales and associated high gradient areas will be more or less enhanced.

d. Contrasting SST and ML depth evolutions

The ML depth evolution during the advective period strongly differs from SST evolution. From Table 1, the RMS value has significantly increased (from 1 m to 1.5 m) and the maximum variation is 12 m (instead of 10 m at $t = 2$ days). The kurtosis value is smaller. Furthermore the normalized gradient variances, σ_n^2, do not display any increase within 8 days, but rather a slight decrease (Table 1). This reveals a tendency for the emergence of the large scales. Therefore the ML depth field evolution within 8 days is characterized by a significant increase of the variance but there is no particular development of the small scales relative to the large scales. The tendency rather seems to favor development of the large scales. On the other hand SST variance does not increase but eventually decreases and the SST field evolution is mainly dominated by the rapid development of energetic small scales relative to the large scales.

An explanation of these different statistical and spectral evolutions is given by the asymptotic states resulting from (10) and (11) (see Section 2c). The asymptotic state of the ML depth field should be close to the isopycnal topography of the deeper layers and therefore should be dominated by the large scales and display a steep spectrum slope (~ -3.5). An estimation of the asymptotic RMS value of h can be given using $h = (\alpha g/N^2)\,\theta_o$ and the RMS value of θ_o. This leads in our study to a value of $\sim$2.56 m, i.e., a larger value than the one at the end of the ML deepening ($\sim$1 m). This explains the tendency observed in the numerical results, i.e., an increase of the ML depth variance with a preference for the appearance of large scales rather than for small scales. On the other hand the rapid development of the small scales observed in the SST evolution characterizes the cascade process of a passive tracer. Furthermore, since the

SST variability resulting from the ML deepening period is characterized by a much steeper spectrum slope than that of the asymptotic state of a passive tracer, the SST field during the advective period is always in a *transient state.*

6. Conclusion

This study has attempted to understand the influence of a subsurface quasi-geostrophic flow on the mesoscale variability of the sea-surface temperature. The situation which is considered has been idealized in order to isolate the main interactions and physical processes involved. In particular, the ML initial conditions are uniform, a spatially uniform and impulsive wind stress is applied and it is assumed that no residual inertial motions exist after the wind stress is stopped.

The first basic process, which can act within two days, is that the impulsive wind-stress acts as photographic developer to unveil at the sea-surface a composite image of the subsurface dynamics, through the mechanism of ML deepening. Depending on the strength of the deepening, the image which is captured in the sea-surface temperature displays a spatial variability which is a linear combination of the subsurface temperature field and of the quasi-geostrophic relative vorticity field. In particular, for strong ML deepening, the SST resembles the subsurface temperature field, with warm sea-surface temperatures located above anticyclonic eddies and cold SST above cyclonic eddies. This result, which was confirmed by the numerical experiments (Section 4), was anticipated analytically by Eq. (9), which contains the most important result concerning SST, whenever a QG flow is present. This result, which relates SST to subsurface temperature and vorticity is akin to the suggestion by Pollard and Regier (1990) that QG potential vorticity is the key to the physics of the structure of the surface layer, although it is proven here that more relevant quantities are actually the depth-integrated components of potential vorticity, which are respectively, the depth-integrated QG vortex stretching (i.e., subsurface temperature) and depth-integrated relative vorticity, and that the dynamics depend on the local Burger number.

During the days after the deepening process has stopped, the evolution of the SST is typical of a transient tracer advected by the QG field: one observes a rapid cascade of its spatial variability from small wavenumbers to large wavenumbers and the emergence of strong thermal fronts and energetic small scales. This evolution mainly depends on the initial injection of the "tracer field" through ML deepening and, most importantly, on the large-scale features that have been injected into the SST field. It should be emphasized that, because of the short time scale involved (a few days), *the field is always in a transient state.* This corresponds in particular to a SST spectrum that can vary significantly within 8 days, ranging from an initial power law of k^{-3} to a final $k^{-1.5}$ value. Such a range of values matches those displayed by satellite images (Gower *et al.*, 1980; Deschamps *et al.*, 1981; Smith *et al.*, 1988). Consequently it seems that, although SST (as well as phytoplankton) generally behaves as a passive tracer stirred by a QG straining field, SST spatial variability can display spectra quite

steeper than the classical "k^{-1}" slope of equilibrium turbulence. In physical space, one can also identify large-scale features such as hammer-heads, which are also commonly observed in satellite images of SST, as resulting from the straining by energetic pairs of QG anticyclonic and cyclonic eddies of the large-scale injected SST features. The passive tracer behavior of SST has already been advocated by authors such as Woods (1988); the novel ingredient here is the recognition of the importance of the entry function of the tracer (through the ML deepening process), namely its large-scale contents due to subsurface temperature or vorticity field and consequently its initial phase shift with respect to the QG advecting flow.

Another variable of importance for the structure of the surface layer is the ML depth. As a result of the ML deepening, the ML depth field is linked to the vorticity and strain fields with larger depths above QG anticyclonic eddies and smaller depth above cyclonic eddies. The latter evolution, when only QG horizontal and vertical advection processes are acting, is characterized by an enhancement of the large-scale features, an increase of the ML depth variance and the disappearance of intermittency. The ML depth evolves toward an asymptotic state that resembles the deeper isopycnal topography, still with larger depths above anticyclonic eddies and smaller depths above cyclonic ones.

The above results show that the ML variability depends on specific dynamical properties of the oceanic mesoscale circulation in the first few hundred meters, namely, *subsurface temperature, relative vorticity,* and the *local ratio of the components of potential vorticity* during the "ML deepening" period; *stirring processes* will determine the SST evolution while *vertical velocity* will steer the ML depth evolution during the "advective" period. Such a strong dependence implies that a detailed knowledge of the oceanic mesoscale subsurface dynamics, and of the large scale features, is prerequisite to an understanding of the emergence and evolution of the ML variability. This is all the more important in that quantitative effects of these dynamical properties are underestimated in the QG approximation: it was shown in both KH88 and the present study that the magnitude of the ML variability is directly proportional to the Rossby number and yet, despite this restriction, the amplitudes of the ML variability for SST and ML depth were found numerically to be non-negligible. It is therefore natural to wonder to which extent these results will be quantitatively enhanced or if they will saturate, for dynamical regimes with Rossby number of order O (1), such as those commonly observed in surface layers data (Pollard and Regier, 1990). Moreover, one may wonder if the mechanisms described here are qualitatively robust to large excursions of the Rossby number. A specific example concerns the asymmetry in the ML entrainment between anticyclonic and cyclonic areas, which was exposed in KH88: QG dynamics does not allow an a priori discrepancy of the dynamical properties of anticyclonic and cyclonic structures of the subsurface flow, while larger Rossby number dynamics will favor such a parity bias of vorticity through differences in stability of the flow. How would this affect the ML entrainment parameterization? All those questions constitute an area for future research.

Most of the above features of the ML response should apply to a more general situation involving in particular nonuniform initial conditions. So let us speculate, for instance, on what governs the SST variability when a nonuniform initial ML depth is considered. This requires mostly the determination of the dominant features of such a nonuniform ML depth field which are given by its large-scale contents. Indeed, from the results of this study, only the large-scale features of the SST field that result from the ML deepening are important for the later SST evolution. From (2), the ML depth variability is affected by QG horizontal and vertical advection, and also by entrainment and inertial pumping. It was shown that both entrainment and QG flow advection (horizontal plus vertical) can produce a ML depth variability, and that large-scale features capture most of the ML depth variance and are close to the deeper isopycnal topography. On the other hand, inertial pumping produces a ML depth variability with variance of the same order of magnitude, but the variance is mainly captured by the small scale features. This is because inertial pumping involves gradients of the vorticity and strain fields (Rubenstein and Roberts, 1986; KH88) and these gradients have a white-noise spectrum at large wavenumbers. Such behavior has been confirmed in several numerical simulations. Therefore the large-scale features of the ML depth should remain unaltered by inertial pumping and would still be close to the deeper isopycnal topography. It is therefore plausible to consider an initial ML depth field in which large scale features are close to the deeper isopycnal topography. Their characteristics are such that the effects of a non-uniform ML depth should enhance the influence of the subsurface temperature on the SST field, through the ML deepening. This should result in a non-negligible increase of the SST variance.

Acknowledgments. This work is supported by IFREMER and the CNRS (through DRET). Calculations reported here were done at the Centre de Calcul Vectoriel pour la Recherche.

REFERENCES

Batchelor, G. K. 1953. Homogeneous Turbulence. Cambridge Univ. Press.

Bennett, A. F. 1984. Relative dispersion: local and nonlocal dynamics. J. Atmos. Sci., *41*, 1881–1886.

D'Asaro, Eric. 1985. The energy flux from the wind to near-inertial motions in the surface mixed layer. J. Phys. Oceanogr., *15*, 1043–1059.

Deschamps, P. Y., R. Frouin and L. Wald. 1981. Satellite determination of the mesoscale variability of the sea surface temperature. J. Phys. Oceanogr., *11*, 864–870.

Elsberry, R. L. and N. T. Camp. 1978. Oceanic thermal response to strong atmospheric forcing I. Characteristics of forcing events. J. Phys. Oceanogr., *8*, 206–214.

Flierl, G. R. 1978. Models of vertical structure and the calibration of two-layer models. Dyn. Atmos. Oceans, *2*, 341–381.

Gower, J. F. R., K. L. Denman and R. J. Holyer. 1980. Phytoplankton patchiness indicates the fluctuation spectrum of mesoscale oceanic structure. Nature, *288*, 157–159.

Hua, B. L. 1990. Absolute Lagrangian dispersion in stratified QG turbulence. J. Fluid Mech., (submitted).

Hua, B. L. and D. B. Haidvogel. 1986. Numerical simulations of the vertical structure of quasi-geostrophic turbulence. J. Atmos. Sci., *43*, 2923–2936.

Klein, P. and B. L. Hua. 1988. Mesoscale variability of the wind-driven mixed layer: influence of a quasigeostrophic flow. J. Mar. Res., *46*, 495–525.

Kraichnan, R. 1974. Convection of a passive scalar by a quasi-uniform random straining field. J. Fluid Mech., *64*, 737–756.

Kunze, Eric. 1985. Near-inertial wave propagation in geostrophic shear. J. Phys. Oceanogr., *15*, 544–565.

Large, W. G., J. C. McWilliams and P. P. Niiler. 1986. Upper ocean thermal response to strong autumnal forcing of the Northeast Pacific. J. Phys. Oceanogr., *16*, 1524–1550.

Lesieur, M. and R. Sadourny. 1981. Satellite-sensed turbulent ocean structure. Nature, *294*, 17.

McWilliams, J. 1984. The emergence of isolated coherent vortices in turbulent flow. J. Fluid Mech., *146*, 21–43.

—— 1989. Statistical properties of decaying geostrophic turbulence. J. Fluid Mech., *198*, 199–230.

Moffatt, H. 1981. A review of turbulence theory. J. Fluid Mech., *73*, 51–87.

Niiler, P. P. 1969. On the Ekman Divergence in an Oceanic jet. J. Geophys. Res., *74*, 7048–7052.

Orszag, S. A. 1971. Numerical simulation of incompressible flows within simple boundaries: accuracy. J. Fluid Mech., *49*, 75–112.

Pedlosky, J. 1987. Geophysical Fluid Dynamics. Springer Verlag, New York. 710 pp.

Pollard, R. T. and L. Regier. 1990. Large potential vorticity variations at small scales in the upper ocean. Nature, (submitted).

Pollard, R. T., P. B. Rhines and R. O. R. Y. Thompson. 1973. The deepening of the wind-mixed layer. Geophys. Fluid Dyn., *4*, 381–404.

POLYMODE. 1986. Local Dynamics Experiment: Introduction and Bibliography. J. Phys. Oceanogr., *16*, 403–652.

Price, J. F., R. A. Weller and R. Pinkel. 1986. Diurnal cycling: observations and models of the upper ocean response to diurnal heating, cooling and wind mixing. J. Geophys. Res., *91*, 8411–8427.

Rhines, P. B. 1983. Lectures in Geophysical Fluid Dynamics. Lectures in Applied Mathematics, *20*, 3–58.

Rubenstein, D. H. and G. O. Roberts. 1986. Scattering of inertial waves by an ocean front. J. Phys. Oceanogr., *16*, 121–131.

Salmon, R. 1980. Baroclinic instability and geostrophic turbulence. Geophys. Astrophys. Fluid Dyn., *15*, 167–211.

Smith, R. C., X. Zhang and J. Michaelsen. 1988. Variability of pigment biomass in the California Current System as determined by satellite imagery 1. Spatial variability. J. Geophys. Res., *93*, 10863–10882.

Weiss, J. 1981. The dynamics of enstrophy transfer in two-dimensional hydrodynamics. Rep. LJI-TN-81-121. La Jolla Institute. La Jolla, California.

Weller, R. A. 1982. The relation of near-inertial motions observed in the mixed layer during the JASIN (1978) experiment to the local wind stress and to the quasi-geostrophic flow field. J. Phys. Oceanogr., *12*, 1122–1136.

Woods, J. D. 1988. Toward a Theory of Biological-Physical Interactions in the World Ocean, B. J. Rothshild, ed., 7–38, Kluwer Academic Publishers.

Received: *21 November, 1989;* revised: *23 August, 1990.*